Gas Evolution and Capacity Fading in $LiFe_xMn_{1-x}PO_4$/Graphite Cells Studied by Neutron Imaging and Neutron Induced Prompt Gamma Activation Analysis

Benjamin Starke,[a,z] Stefan Seidlmayer,[b] Michael Schulz,[b] Alexander Dinter,[a] Zsolt Revay,[b] Ralph Gilles,[b] and Karl-Heinz Pettinger[a]

[a]*Technology Center for Energy, University of Applied Sciences Landshut, 84036 Landshut, Germany*
[b]*Heinz Maier-Leibnitz Zentrum (MLZ), Technische Universität München, 85748 Garching, Germany*

The gas evolution in LFP/graphite and LFMP/graphite cells during the formation has been analyzed via neutron imaging (NI). The results show that in LFMP/graphite cells approximately 30% more gas is generated in comparison to LFP/graphite and stronger gas evolution is associated with the presence of Mn. For the LFP/graphite cell two different linear phases in gas evolution rate can be detected while LFMP/graphite cells reveal an additional phase. In both full-cells a distinct relation between gas evolution and electrode potentials has been determined. Additional neutron induced Prompt Gamma Activation Analysis (PGAA) measurements were carried out in order to correlate long-term Mn dissolution and capacity retention. Long-term cycling showed higher capacity retention for the LFMP/graphite cells. The results of PGAA prove that Mn dissolution decreases rapidly with increased cycle number and the Mn dissolution rate of LFMP is far below values observed for oxide-type cathode materials. Long-term cycling showed that the negative effects of higher irreversible capacity loss in the formation step and more gas evolution of LFMP/graphite cells in comparison to LFP/graphite cells is compensated after several cycles due to higher capacity retention.
 [DOI: 10.1149/2.0011802jes]

Manuscript submitted November 6, 2017; revised manuscript received December 15, 2017. Published December 30, 2017.

Due to their high energy density and operating voltage lithium-ion batteries are a key technology for mobile applications such as communication devices and electric vehicles.[1–3] But also stationary energy storage systems are increasingly developed under usage of lithium-ion technology. Those stationary storage systems range from small (e. g. home storage for photovoltaic plants) to large scale applications (grid stabilization).[4–6] Especially in cases of high capital expenditures, consumers and operators expect a long battery lifetime in terms of capacity and charge and discharge characteristics.

Applications like home energy storage require high operational safety standards. These requirements are met by the cathode active material $LiFePO_4$ (LFP), which has first been described in 1997.[7] Phospho-olivines such as LFP provide good operational characteristics in terms of thermal runaways and are furthermore environmentally friendly and cost-efficient.[8–10] By partial substitution of Fe by Mn in $LiFePO_4$, the isostructural $LiFe_xMn_{1-x}PO_4$ is obtained. It features a higher operating voltage due to the redox couple Mn^{2+}/Mn^{3+} at approximately 4.2 V vs. Li/Li^+ in comparison to Fe^{2+}/Fe^{3+} at approximately 3.5 V vs. Li/Li^+. The different voltages of the redox couples can be found as characteristic voltage plateaus in the charge and discharge curves of $LiFe_xMn_{1-x}PO_4$[11–14].

Benefits of higher cell voltage and energy density of $LiFe_xMn_{1-x}PO_4$-based batteries are accompanied by problems caused by Mn dissolution. Dissolved Mn results in capacity fading caused by parasitic processes such as electrolyte decomposition and insertion into the anodic SEI layer.[15,16] Dissolution of Mn is not a selective problem of $LiFe_xMn_{1-x}PO_4$ and has been observed for other cathode materials like spinel-type $LiNi_{0.5}Mn_{1.5}O_4$.[17]

The dissolution of Mn from LFMP as such has recently been investigated and a strong correlation between dissolved Mn and traces of H_2O contamination in the electrolyte has been stated. It has also been found that in case of LFMP there is no selective dissolution of Mn since Fe is dissolved as well and the Mn/Fe ratio in the electrolyte and the active material is equal.[18]

Another study has shown that transition metal dissolution also occurs in oxide-type active materials such as layered Nickel-Manganese-Cobalt oxide based active materials (NMC).[19] In case of NMC all present transition metals Ni, Mn and Co dissolve in the electrolyte and migrate to the anodic graphite. But while Ni and Co remain in the oxidation state +II, Mn is reduced to Mn^0 and subsequently re-oxidized to Mn^{2+} under continuous electrolyte reduction and loss of active lithium. This result and the proposed Mn^0/Mn^{2+} redox cycle highlight the special influence of Mn in the context of capacity fading and cell performance. The result of this study is of importance for LFMP/graphite full-cells because it describes a Mn-related mechanism on the anode independently from the cathode active material.[20]

For the in situ visualization of manganese dependent initial gas evolution in lithium-ion batteries X-rays are of limited suitability. The scattering cross section of X-rays increases with the number of electrons of an atom.[21] Thus, lithium as it is present in the electrolyte is difficult to detect. In contrast, the scattering cross section of neutrons does not correlate with the atomic number but is influenced by the properties of the atomic nuclei and varies for each element.[22] Neutrons are significantly attenuated by lithium and hydrogen. In contrast, aluminum as it is used in the pouch foil of a lithium ion battery is mainly transparent for neutrons.[23] These properties make neutron-based imaging the method of choice for in situ visualization of gas evolution in Li-containing systems such as lithium-ion batteries.[24]

Michalak et al. have demonstrated the suitability of neutron imaging for in operando observation of gas evolution in lithium ion batteries.[25] Analyses of the evolved gas volume of different anode/cathode combinations lead to the result that $LiNi_{0.5}Mn_{1.5}O_4$/graphite cells contain the highest amount of gas possibly caused by the presence of Mn which is dissolved from the active material. This suggests a stronger gas evolution in LFMP/graphite cells in comparison to LFP/graphite cells.

The versatile technique of neutron imaging has also been successfully applied on other aspects related to lithium-ion batteries. Studies range *inter alia* from electrolyte filling to lithiation processes and active material synthesis.[26–28]

In the present study, we provide a direct and detailed comparison of LFP/graphite and LFMP/graphite full-cells in order to determine the influence of manganese on the initial gas evolution by means of neutron imaging (NI). Additionally, we use Prompt Gamma Activation Analysis (PGAA) to understand the long-term development of Mn dissolution and its relation to capacity retention.

[z]E-mail: benjamin.starke@haw-landshut.de

Experimental

Sample preparation.—Development-grade LFP and LFMP have been used as starting material for this experiment. Both powder samples were processed to solvent-based slurries. For slurry preparation PVDF (Solef 5130, Solvay) was dissolved in N-methyl-2-pyrrolidone (NMP, Roth) and mixed with LFP or LFMP and carbon black (Super C65, TIMCAL). The constituents were then dispersed by using a dissolver (DISPERMAT, VMA GETZMANN GmbH) for 25 minutes at 3500 rpm. The obtained slurries were degassed in a planetary centrifugal mixer (THINKY) for 4 minutes at 2200 rpm and cast on a carbon-coated aluminum current collector. The cathodes were dried at 110°C under vacuum for 12 hours. The solid content fractions of the cathodes were 88.0 wt% LFP or LFMP, 6.0 wt% carbon black and 6.0 wt% PVDF.

For the NI experiment LFP and LFMP cathodes were assembled as single-layer full-cells by using an inorganically filled PVDF separator and anodes consisting of carbon black (Super C65, TIMCAL,) (4.0 wt%), carboxymethyl cellulose (MAC 200 HC, Sunrose, Nippon Paper Industries Co., Ltd.) (1.8 wt%) and SBR (BM-400B, ZEON) (2.8 wt%). Full-cells were filled with 1.5 mL of LP 50 (1 M LiPF6 in EC:EMC (1:1 wt%), BASF).

Complementing to the NI experiment Swagelok T-cells (3-electrode setup) were assembled in order to record the individual potentials of the cathode and anode vs. Li/Li^+ during the charge process. This allows a more profound correlation of gas evolution and electrochemical processes during the formation step. Cathodes and anodes were the same as used for the NI experiment. For the T-cells electrodes with a diameter of 10 mm were punched out. The glass fiber separator (Sartorius AG) had a diameter of 12 mm and 180 µL of LP 50 were used for the T-cells. A lithium foil (GELON LIB) was used as reference electrode and all T-cells were assembled in an argon-filled glove box (M. Braun Inertgas-Systeme GmbH). T-cells were charged in the same way as the full-cells during the NI experiment as described in section Neutron imaging (NI) and data processing.

PGAA was carried out to study the long-term manganese dissolution from LFMP and migration to the anode. Therefore, four different anode samples were prepared. The first sample was a fresh anode in order to determine residual traces of Mn in the copper current collector foil. For obtaining the other three anode samples full-cells were prepared for the NI experiment. One of the full-cells was only formed with a charge rate of C/10 up to 4.3 V with a potential hold until the current dropped below C/20 and a discharge rate of C/10 to 2.0 V. Two further full-cells were formed in the same way and additionally charged at a 1 C-rate up to 4.3 V until the current dropped below C/20 and discharged to 2.0 V for 100 and 200 cycles, respectively. Subsequently, all three full-cells were opened and the anodes were extracted. All samples for the PGAA measurement were punched out of the anodes and had a diameter of 10 mm.

Neutron imaging (NI) and data processing.—NI experiments were performed on the instrument ANTARES at the neutron source FRM II at the Heinz Maier Leibnitz Zentrum (MLZ) in Garching, Germany.[29,30]

In situ observation of the initial gas evolution in LFP/graphite and LFMP/graphite full-cells was carried out by charging the cells at a rate of C/10 up to 3.7 V or 4.3 V, respectively, and a potential hold until the current dropped below C/20. The potentiostat which was used for full-cell charging had to be placed in direct proximity to the open beam and was therefore protected against radiation by using lead bricks and boron-filled rubber mats. During the full-cell charging images were recorded every 25 seconds with an exposure time of 5 seconds resulting in one image every 30 seconds.

The images were recorded with an Andor IkonL 2048 × 2048 pixel cooled scientific CCD camera which viewed a 100 µm thick LiF:ZnS scintillation screen via an f = 100 mm lens. The effective pixel size of the setup was ~70 µm. A beam collimation of L/D = 500 was used, resulting in a neutron flux of $\approx 6.4 \cdot 10^7$ $cm^{-2}s^{-1}$.

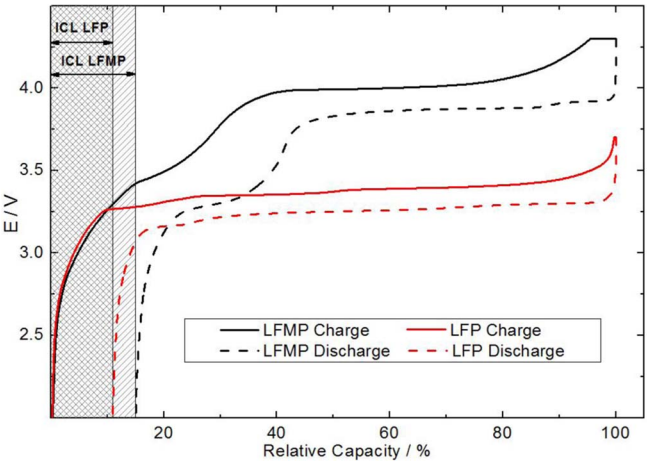

Figure 1. Charge and discharge curves of the formation cycle for LFP/graphite and LFMP/graphite cells. Grey areas on the left side illustrate the irreversible capacity loss (ICL) measured after the formation step.

To evaluate the data, the images were normalized to an image taken with the cell mounted in front of the detector but prior to charging. Consequently, only changes in the distribution of the electrolyte are visible in these normalized images, while structural materials are not observed. The data were subsequently smoothed by applying a 5 × 5 pixel median filter. The obtained transmission values are given as:

$$T = \frac{I_{data}}{I_{initial}} = e^{-\mu_{electrolyte} \cdot d_{diff}}$$

Where I_{data} and I_{inital} are the images acquired during and before charging, respectively, $\mu_{electrolyte}$ is the linear attenuation coefficient of the electrolyte which was assumed to be constant and d_{diff} is the change in electrolyte thickness at one position. The negative natural logarithm of the transmission values in these images was taken in order to determine the effective change in electrolyte thickness due to the gas formation and electrolyte displacement within the cell. As a measure of the produced gas volume, the sum over all pixels in the image with a gray value smaller than 0 (i.e. less electrolyte thickness than in the initial state) was taken. This value is linearly proportional to the gas volume and was plotted in Figure 3 as a function of SOC.

Prompt gamma activation analysis (PGAA).—The samples were analyzed at the PGAA facility at Heinz Maier-Leibnitz Zentrum (MLZ) in Garching, Germany.[31] PGAA is based on the radiative neutron capture process: after the neutron capture, the atomic nuclei release the excitation energy in the form of characteristic gamma rays whose energies identify the elements, while the elemental composition can be determined from their intensities.[32] The samples in our experiments were irradiated in a cold neutron beam with a flux of $\approx 1.35 \cdot 10^{10}$ $cm^{-2}s^{-1}$ for about two hours. The prompt gamma rays were detected with a high-purity germanium (HPGe) detector with a relative efficiency of 60% surrounded by a bismuth germanate scintillator annulus as a Compton suppressor.[33] The spectra were collected using an ORTEC Dspec-50 spectrometer. The gamma spectra were evaluated using the Hypermet-PC program, and the list of peak energies and areas were statistically analyzed, then fit to elemental data in the spectroscopy database, as described by Z. Révay.[34]

Results and Discussion

A first difference in electrochemical characteristics between LFP/graphite and LFMP/graphite cells was observed in the formation. The formation step of a LFP/graphite and LFMP/graphite cell is illustrated in Figure 1. In the LFP/graphite cell no significant CV-phase

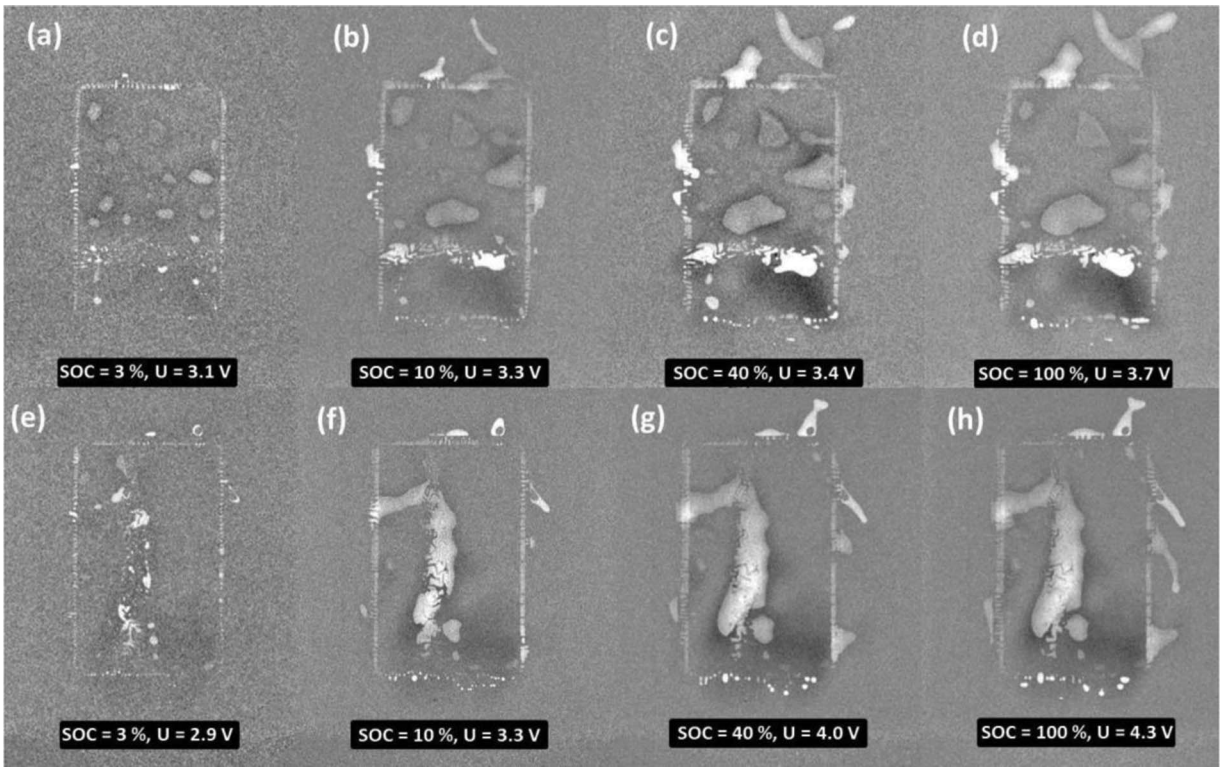

Figure 2. Neutron images of LFP/ graphite and LFMP/graphite full-cells recorded during the formation step at different states of charge (SOC) and cell voltages as shown in the inserted text boxes. (a)-(d) images of the LFP/graphite full-cell; (e)-(h) images of the LFMP/graphite full-cell. Images were obtained by normalizing the respective imageto the first recorded image at the beginning of the formation step (see Neutron imaging (NI) and data processing for more details on data processing). Evolved gas is visible in the form of bright areas where the electrolyte has been displaced, whereby the brightness (gray value) of an area correlates to the degree of displacement.

is visible. In contrast, the LFMP/graphite cell requires a CV-phase which transfers ≈ 5% of the total charge before the current dropped below C/20.

In Figure 1 the irreversible capacity losses (ICL) observed after the formation step are highlighted by the gray areas on the left side of the graph. The LFP/graphite cell lost 10.6% of its capacity, while the LFMP/graphite cell lost 15.0%. Since the cathode active material is the only variation between both T-cells, this difference of 4.6% is most probably caused by the presence of Mn in LFMP.

Figure 2 provides a visual comparison of the in operando gas evolution inside the LFP/graphite and LFMP/graphite full-cell. The images represent different states of charge (SOC) and evolved gas is visible in the form of bright areas where the electrolyte has been displaced, whereby the brightness (gray value) of an area correlates to the degree of displacement.

As Figures 2a and 2e illustrate, the initial formation of gas bubbles takes place at the edges of the electrodes, making their shape visible. Since no external pressure was applied on the full-cells, generated gas bubbles can move freely and accumulate at different positions inside the pouch of the cells. Since the three-layered pouch foil of the battery (PP-Al-PET) is relatively stiff, the gas is partially hindered to move to the upper section of the pouch bag. As the Figures 2c and 2d (LFP/graphite cell) as well as Figures 2g and 2h (LFMP/graphite cell) indicate, the gas volume remains nearly constant from SOC = 40% to SOC = 100%.

For a more precise analysis of the evolved gas volume in the full-cells, the data of NI was processed as described in the Experimental section. The results of the data processing are visualized in Figure 3. In order to better correlate gas evolution and electrode potentials, voltages shown in Figure 3 were obtained by formation of LFP/graphite and LFMP/graphite in a T-cell setup. Remarkable positions of the gas volume curves are indicated by asterisks. For the LFP/graphite cell the last data set representing the gas volume was set to 100%. All data obtained for the LFMP/graphite cells was set into relative relation to this value in order to provide a direct comparability.

The results of the LFP/graphite cell are shown in Figure 3a. The LFP cathode directly reaches and remains on its Fe^{2+}/Fe^{3+} redox plateau over the formation process, while the potential of the graphite anode drops below 1.0 V vs. Li/Li^+. It can also be seen that gas is immediately generated at the beginning of the cell formation with a constant rate. In this region labelled as Section I the gas volume increases linearly until the potential of the anode reaches approximately 0.2 V vs. Li/Li^+. At this potential the voltage curve of the anode proceeds on a horizontal plateau which is characteristic for the beginning formation of LiC_{18}.[35] Simultaneously, in Section III the slope of the gas volume curve decreases after the red asterisk and continues linearly over the remaining cell formation process until the end of the charging. At the red asterisk approximately 75% of the overall gas volume has been evolved, while the SOC of the cell has only reached 12%. The clear correlation between anodic potential and change in gassing rate highlights the anodic influence on gas evolution. The results indicate that SEI formation and gassing are mainly completed when lithium insertion into graphite reaches the beginning intercalation state of LiC_{18}. Ongoing gassing is probably caused by continuous but moderate SEI formation.

Figure 3b illustrates the results for the LFMP/graphite cell. As observed for the LFP/graphite cell, gas evolution also starts right at the beginning of the formation and continues at a constant rate until the anode potential reaches its first plateau at 0.2 V vs. Li/Li^+ (red asterisk marks the end of Section I). A comparison of the gas volumes in both cells at this point states that the LFMP/graphite cell tends to have a higher gassing rate. In relation to the final gas volume in the LFP/graphite cell the gas volume in the LFMP/graphite cell reached approx. 90% while it is 75% in the case of LFP/graphite at the point marked by the red asterisk. Besides this remarkable difference in initial gas evolution another difference can be observed. In the case

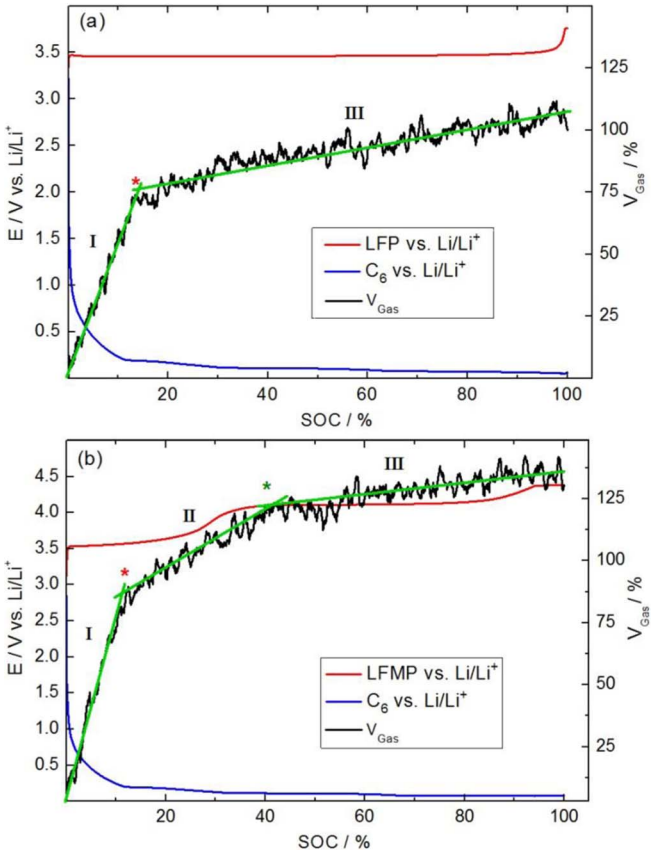

Figure 3. Gas volume calculated on the basis of the NI data. Individual electrode potentials were obtained by T-cells measurements. (a) Data for LFP/graphite cell; (b) Data for LFMP/graphite cell. Remarkable positions are highlighted with asterisks. Different sections of the gas curve are indicated with Roman numerals. Green lines as a guide to the eye show the linearity of the gas evolution process and the different gas evolution rates. The division into sections is based on the empirical results of the neutron imaging experiment.

of the LFP/graphite cell only two linear sections of the gas volume curve can be distinguished. But for the LFMP/graphite cell three linear sections can be identified. The first one is identical for both cells and ends at the anodic potential of 0.2 V vs. Li/Li^+ (red asterisk in Figures 3a and 3b, respectively). The Section II is characteristic only for the LFMP/graphite cells and is located between the red and green asterisk. In this region the gas evolution rate decreases relative to Section I but is still elevated. Within Section II the potential of the cathode rises from 3.5 V vs. Li/Li^+ (Fe^{2+}/Fe^{3+} redox plateau) to 4.1 V vs. Li/Li^+ (Mn^{2+}/Mn^{3+} redox plateau). The end of section II is marked by the green asterisk which correlates strongly with reaching of the Mn^{2+}/Mn^{3+} redox plateau. The third linear section of the gas curve (III) has a similar slope as section III of the gas curve obtained for the LFP/graphite cell. Altogether, in relation to the LFP/graphite cell the final gas volume in the LFMP/graphite cell is 30% higher.

The only difference between both cells is the presence of Mn in the LFMP/graphite cell and it is therefore the only explanation for the different gas evolution characteristics and final gas volumes. The reduced but still elevated gas evolution rate in section II of the LFMP/graphite cell can be explained by Mn insertion into the anodic SEI layer. The deposited Mn holds up the electric conductivity between the graphite and the electrolyte causing ongoing electrolyte reduction to gaseous products. Deposited Mn also leads to a thicker SEI layer which comes along with higher active lithium consumption and irreversible capacity loss.[17] It also seems plausible that as more SEI has to be generated in the presence of Mn depositing into the SEI layer, the more gas is produced, clearly corresponding to the observation of increased gassing rate and elevated total gas generation of LFMP relative to LFP.

Table I. Results of the PGAA analysis given in relation to Cu of the anode current collector in the sample.

		Mn content relative to Cu in		
Cell-No.	Number of cycles	ppm	µg/mg	Rel. uncertainty
1	0	2.1	0.0018	10%
2	1	16	0.0138	6%
3	100	157	0.1357	5%
4	200	225	0.1945	4%

Again referring to the gas volume curves in Figure 3, we consider the sections I and III of the LFP/graphite cell and the sections I and III of the LFMP/graphite cell to be identical in terms of the underlying mechanism. The additional section II in Figure 3b therefore seems to be characteristic for the LFMP/graphite cell and the underlying mechanism contributes significantly to the observed higher final gas volume. Our results indicate a correlation between reduced gas evolution rate and incipient Mn^{2+}/Mn^{3+} redox reaction. The exact reasons for this finding and the underlying electrochemical processes are subject to further detailed research. For clarification, electrolyte decomposition and gas evolution occur in nearly all lithium-ion batteries using graphite as anode material. The reason is found in the intercalation voltage of lithium into graphite, which is below the window of electrochemical stability of commonly used carbonate electrolytes.[36] As a consequence, during the first cycle a Solid Electrolyte Interface (SEI) is formed on the graphite surface under consumption of lithium from decomposed electrolyte and the cathode active material.[37] The SEI-layer consists of compounds such as Li_2O, LiF and Li_2CO_3.[38] Gaseous compounds which are formed can be for example CO_2 and H_2.[39,40] Detailed discussion of electrolytes and occurring reactions is provided in References 41 and 42. The thickness of the SEI-layer, loss of active lithium and evolved gas can be increased, if the process of SEI-formation is extended by insertion of metal ions (e. g. Mn) into the SEI-layer.[17]

In addition to the initial gas evolution PGAA measurements were carried out in order to quantify the Mn dissolution at different cycle numbers. Table I summarizes the results of the PGAA measurements. According to Saulnier et al. Fe and Mn dissolve in the electrolyte in the same ratio as they are present in LFMP.[18] This result could not be confirmed in our experiment since the Fe concentration was below the specific detection limit for PGAA analysis.

In consideration of the cathode coating thickness of the cells 2, 3 and 4, the active material content and Mn/Fe ratio in LFMP, the values given in Table I can be converted into values representing the loss rate of Mn in relation to the total Mn content in LFMP per cycle. In this way, the long-term evolution of Mn dissolution during cycling can be better illustrated. The results of this conversion are shown in Figure 4.

In Figure 4, the loss of Mn from LFMP is strongly elevated during the first cycle (1.02 ppm). In comparison to the formation step, the loss rate per cycle drops down to 0.09 ppm during the cycles 2–100. This value represents the average loss rate over 99 cycles. During the cycles 101–200 the loss rate decreases further to 0.04 ppm per cycle. The results show that Mn dissolution takes mainly place in the beginning and decreases significantly within ongoing cycling. The Mn loss per cycle appears to follow a 1/x or similar function with decreasing negative slope.

Although it has to be taken into account that besides parasitic reactions of dissolved Mn with the electrolyte and SEI, the loss of Mn itself causes a capacity loss of the active material. But Figure 4 demonstrates that the loss rates of Mn are very low and the dissolution from the active material *as such* does not significantly elevate capacity fading rates.

Each dissolved Mn^{2+}-ion causes an excess of two negative charges in LFMP which has to be compensated due to the mandatory charge balance in the active material. The charge balance could either be realized by providing two positive charges (e.g. via oxidation) or loss

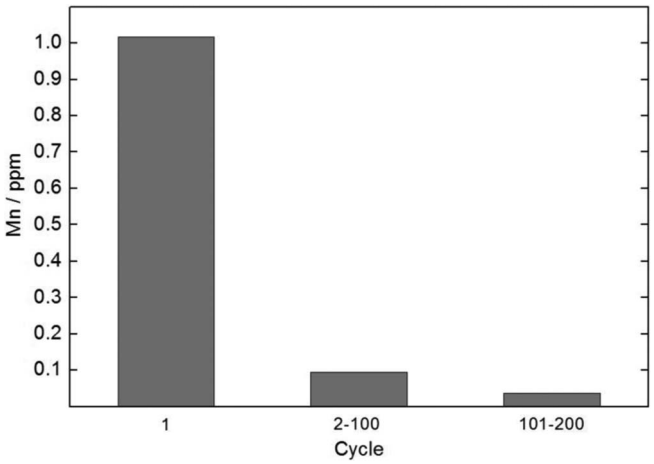

Figure 4. Loss of Mn per cycle in ppm of the total Mn present in LFMP.

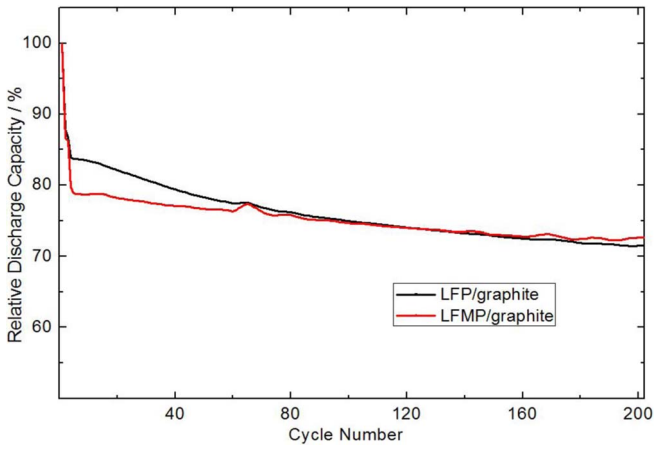

Figure 5. Capacity retention of LFP/graphite and LFMP/graphite full-cells over 200 cycles at a 1 C-rate. Left side of the graph illustrates the ICL upon formation at 0.1 C.

of two negative charges (e.g. oxygen release). But an oxygen release is very unlikely due to the strong covalent P-O bonding in PO_4^{3-}.[43] Thus charge balance is likely provided by oxidation of two Mn^{2+}-ions to Mn^{3+}-ions. During the charge process Li^+-ions de-intercalate from LFMP while Mn^{2+} is oxidized to Mn^{3+}. This oxidation is no longer possible since Mn is already present in the oxidation state +3 and thus two Li^+-ions are prevented from de-intercalation. In $LiFe_xMn_{1-x}PO_4$ Mn occurs in the oxidation states +2 and +3.[44] To our best knowledge, a redox couple Mn^{3+}/Mn^{4+}, which might in this case still allow lithium de-intercalation, does not exist for $LiFe_xMn_{1-x}PO_4$ – in contrast to the spinel-type NMC material. In consideration of the third Li^+-ion, which is immobilized due to the dissolution of one Mn^{2+}-ion, three active lithium ions are lost upon dissolution of one Mn^{2+}-ion. It might theoretically be possible that Fe^{2+} is instead oxidized to Fe^{3+} in order to recover charge balance upon Mn^{2+} dissolution. But this question is of secondary importance for the present study since it would similarly result in the loss of three active lithium ions per lost Mn^{2+}.

Although Mn dissolution as such causes a 3-fold loss of active lithium, it still contributes only marginally to the observed capacity fading. Summing up and even triplicating the values of deposited Mn given in Figure 4 results in an active lithium loss of mere 41.8 ppm after 200 cycles. Obviously Mn dissolution *as such* is uncritical in terms of a direct cause of capacity loss.

The authors Seidlmayer and Gilles together with Buchberger et al. have also recently published an investigation of Mn dissolution from the active material NMC.[19] In this study PGAA was used for measuring extracted anodes with an internal Cu standard. This study has found up to 3.5 µg Mn per mg Cu after 300 cycles (cutoff voltage 4.6 V, 25°C). In comparison, in the present study we measured 0.19 µg Mn per mg Cu after 200 cycles, which equals an 18 times lower value. Considering cathode areal loading in the above mentioned study was approximately twice as high as in the present study, but Mn content in NMC (33 at%) at the same time roughly half of the amount of Mn in our LFMP (67 at%). This means that the total amount of Mn present in the cathodes is roughly equal. The PGAA measurements in Reference 19 were carried out after 300 instead of 200 cycles. Nonetheless the enhancement factor of 18 between the two studies shows how relatively low the Mn dissolution rate of the investigated LFMP is in comparison to the NMC material.

Long-term cycling was carried out in order to correlate capacity fading and Mn dissolution determined via PGAA measurement. The result of the long-term cycling is shown in Figure 5. The initial charge capacity observed during the formation step was set to 100% and the subsequently measured discharge capacities were set into relation to this value in order to visualize the formation loss.

As illustrated in Figure 5, the irreversible capacity loss (ICL) of LFMP/graphite full-cells is higher and thus the discharge capacity is lower at the beginning of the cycling. Remarkably though, the fading rate of the LFMP/graphite full-cells is lower which causes a convergence and crossing of the discharge capacity curves after approx. 130 cycles. Due to the higher capacity retention during the cycling, the initial disadvantage of higher irreversible capacity loss of LFMP/graphite full-cells is compensated. Since 130 cycles is a relatively low number of cycles for battery-based applications, it can be stated that LFMP/graphite is a more favorable system in terms of total battery lifetime. Our results indicate that Mn dissolution in the LFMP/graphite system has merely an initial impact on the cell capacity. Mn dissolution rates found in other studies on spinel-type NMC and LNMO exceed largely the values we have measured for LFMP via PGAA.[19,45]

Therefore, we conclude that in comparison to other cathode active materials Mn is very stable bound in the LFMP host structure. High capacity retention as illustrated in Figure 5 also states that continuous, but strongly decreasing Mn deposition on the anode as shown via PGAA is non-critical in terms of parasitic processes. After 200 cycles at a 1 C-rate LFMP/graphite full-cells provide a 1% higher discharge capacity. This is only a slight difference to the LFP/graphite cells but improved performance of LFMP/graphite cells is expected to become more distinct with increased cycle number.

Conclusions

In this experiment we have demonstrated the suitability of NI for identifying different characteristics of gas evolution caused by the presence of Mn in LFMP in comparison to LFP. In LFMP/graphite full-cells, a 30% higher gas volume was measured after the first charge which can only be explained by Mn-induced parasitic processes. Furthermore, PGAA measurements have proven that the Mn dissolution rate decreases rapidly with increased cycle number and the dissolution rate is low in comparison to other Mn-containing active materials such as NMC.

Long-term cycling experiments showed that the initial disadvantage of LFMP/graphite cells due to a higher ICL in comparison to LFP/graphite is compensated with increased cycle number due to a lower capacity fading rate of LFMP/graphite cells resulting in a higher discharge capacity after 130 cycles.

Future experiments will be focused on a higher time resolution of Mn dissolution. A more precise understanding of the correlation between Mn dissolution, gas evolution and electrode potentials should be feasible by interrupting cell formation at different cell potentials and subsequent PGAA measurements. This method provides data on an intra-cycle level and might help to attain information for improved formation procedures of LFMP-based lithium-ion batteries.

Acknowledgment

The authors gratefully acknowledge the Heinz Maier-Leibnitz Zentrum (MLZ) for granting us beam time at the instruments ANTARES and PGAA. This work was supported by the Bavarian Ministry of Education and Culture (grant number: VIII.2-F1116.LA/13/3). One of the authors (S. Seidlmayer) thanks the German Federal Ministry of Education and Research (project number: 03XP0081) under the auspices of the ExZellTUM 2 project.

References

1. K. Mizushima, P. C. Jones, P. J. Wiseman, and J. B. Goodenough, *Materials Research Bulletin*, **15**(6), 783 (1980).
2. M. Hu, X. Pang, and Z. Zhou, *Journal of Power Sources*, **237**, 229 (2013).
3. L. Lu, X. Han, J. Li, J. Hua, and M. Ouyang, *Journal of Power Sources*, **226**, 272 (2013).
4. B. Dunn, H. Kamath, and J. -M. Tarascon, *Science (New York, N. Y.)*, **334**(6058), 928 (2011).
5. M. Naumann, R. C. Karl, C. N. Truong, A. Jossen, and H. C. Hesse, *Energy Procedia*, **73**, 37 (2015).
6. D. Di Lecce, R. Verrelli, and J. Hassoun, *Green Chem*, **19**, 3442 (2017).
7. A. K. Padhi, *J. Electrochem. Soc.*, **144**(4), 1188 (1997).
8. M. Takahashi, H. Ohtsuka, K. Akuto, and Y. Sakurai, *J. Electrochem. Soc.*, **152**(5), A899 (2005).
9. L. -X. Yuan, Z. -H. Wang, W. -X. Zhang, X. -L. Hu, J. -T. Chen, Y. -H. Huang, and J. B. Goodenough, *Energy Environ. Sci.*, **4**(2), 269 (2011).
10. A. W. Golubkov, D. Fuchs, J. Wagner, H. Wiltsche, C. Stangl, G. Fauler, G. Voitic, A. Thaler, and V. Hacker, *RSC Adv*, **4**(7), 3633 (2014).
11. G. Li, Y. Kudo, K. -Y. Liu, H. Azuma, and M. Tohda, *J. Electrochem. Soc.*, **149**(11), A1414 (2002).
12. N. V. Kosova, E. T. Devyatkina, A. I. Ancharov, A. V. Markov, D. D. Karnaushenko, and V. K. Makukha, *Solid State Ionics*, **225**, 564 (2012).
13. N. N. Bramnik, K. G. Bramnik, K. Nikolowski, M. Hinterstein, C. Baehtz, and H. Ehrenberg, *Electrochem. Solid-State Lett.*, **8**(8), A379 (2005).
14. J. Molenda, W. Ojczyk, K. Swierczek, W. Zajac, F. Krok, J. Dygas, and R. Liu, *Solid State Ionics*, **177**(26-32), 2617 (2006).
15. I. A. Shkrob, A. J. Kropf, T. W. Marin, Y. Li, O. G. Poluektov, J. Niklas, and D. P. Abraham, *J. Phys. Chem. C*, **118**(42), 24335 (2014).
16. J. A. Gilbert, I. A. Shkrob, and D. P. Abraham, *J. Electrochem. Soc.*, **164**(2), A389 (2017).
17. Nicholas P. W. Pieczonka, Z. Liu, P. Lu, K. L. Olson, J. Moote, B. R. Powell, and J. -H. Kim, *J. Phys. Chem. C*, **117**(31), 15947 (2013).
18. M. Saulnier, A. Auclair, G. Liang, and S. B. Schougaard, *Solid State Ionics*, **294**, 1 (2016).
19. I. Buchberger, S. Seidlmayer, A. Pokharel, M. Piana, J. Hattendorff, P. Kudejova, R. Gilles, and H. A. Gasteiger, *J. Electrochem. Soc.*, **162**(14), A2737 (2015).
20. J. Wandt, A. Freiberg, R. Thomas, Y. Gorlin, A. Siebel, R. Jung, H. A. Gasteiger, and M. Tromp, *J. Mater. Chem. A*, **4**(47), 18300 (2016).
21. B. L. Henke, E. M. Gullikson, and J. C. Davis, *Atomic Data and Nuclear Data Tables*, **54**(2), 181 (1993).
22. F. Hippert, *Neutron and X-ray spectroscopy*, Dordrecht, Springer (2006).
23. V. F. Sears, *Neutron News*, **3**(3), 26 (2006).
24. M. Kamata, T. Esaka, S. Fujine, K. Yoneda, and K. Kanda, *Journal of Power Sources*, **68**(2), 459 (1997).
25. B. Michalak, H. Sommer, D. Mannes, A. Kaestner, T. Brezesinski, and J. Janek, *Scientific reports*, **5**, 15627 (2015).
26. T. Knoche, V. Zinth, M. Schulz, J. Schnell, R. Gilles, and G. Reinhart, *Journal of Power Sources*, **331**, 267 (2016).
27. F. Sun, H. Markötter, I. Manke, A. Hilger, S. S. Alrwashdeh, N. Kardjilov, and J. Banhart, *Applied Surface Science*, **399**, 359 (2017).
28. S. Takai, *Solid State Ionics*, **123**(1–4), 165 (1999).
29. M. Schulz and B. Schillinger, *JLSRF*, **1** (2015).
30. E. Calzada, F. Gruenauer, M. Mühlbauer, B. Schillinger, and M. Schulz, *Nuclear Instruments and Methods in Physics Research Section A: Accelerators, Spectrometers, Detectors and Associated Equipment*, **605**(1–2), 50 (2009).
31. Z. Revay, *JLSRF*, **1** (2015).
32. R. M. Lindstrom, *Journal of research of the National Institute of Standards and Technology*, **98**(1), 127 (1993).
33. Z. Révay, P. Kudějová, K. Kleszcz, S. Söllradl, and C. Genreith, *Nuclear Instruments and Methods in Physics Research Section A: Accelerators, Spectrometers, Detectors and Associated Equipment*, **799**, 114 (2015).
34. Z. Révay, *Analytical chemistry*, **81**(16), 6851 (2009).
35. M. Winter, J. O. Besenhard, M. E. Spahr, and P. Novák, *Adv. Mater.*, **10**(10), 725 (1998).
36. D. Aurbach, Y. Talyosef, B. Markovsky, E. Markevich, E. Zinigrad, L. Asraf, J. S. Gnanaraj, and H. -J. Kim, *Electrochimica Acta*, **50**(2–3), 247 (2004).
37. E. Peled and S. Menkin, *J. Electrochem. Soc.*, **164**(7), A1703 (2017).
38. E. Peled, *J. Electrochem. Soc.*, **144**(8), L208 (1997).
39. R. Bernhard, M. Metzger, and H. A. Gasteiger, *J. Electrochem. Soc.*, **162**(10), A1984 (2015).
40. A. Wuersig, W. Scheifele, and P. Novák, *J. Electrochem. Soc.*, **154**(5), A449 (2007).
41. S. J. An, J. Li, C. Daniel, D. Mohanty, S. Nagpure, and D. L. Wood, *Carbon*, **105**, 52 (2016).
42. Q. Li, J. Chen, L. Fan, X. Kong, and Y. Lu, *Green Energy & Environment*, **1**(1), 18 (2016).
43. C. Julien, A. Mauger, K. Zaghib, and H. Groult, *Inorganics*, **2**(1), 132 (2014).
44. K. -W. Nam, W. -S. Yoon, K. Zaghib, K. Yoon Chung, and X. -Q. Yang, *Electrochemistry Communications*, **11**(10), 2023 (2009).
45. J. -H. Kim, N. P. W. Pieczonka, Z. Li, Y. Wu, S. Harris, and B. R. Powell, *Electrochimica Acta*, **90**, 556 (2013).